Nonlocal magnon-polaron transport in yttrium iron garnet

L. J. Cornelissen, K. Oyanagi, T. Kikkawa, Z. Qiu, T. Kuschel, G. E. W. Bauer, B. J. van Wees,
and E. Saitoh

Nonlocal magnon-polaron transport in yttrium iron garnet

L.J. Cornelissen,[1, *] K. Oyanagi,[2, *] T. Kikkawa,[2, 3] Z. Qiu,[3] T. Kuschel,[1] G.E.W. Bauer,[1, 2, 3, 4] B.J. van Wees,[1] and E. Saitoh[2, 3, 4, 5]

[1]*Physics of Nanodevices, Zernike Institute for Advanced Materials, University of Groningen, Nijenborgh 4, 9747 AG Groningen, The Netherlands* [†]
[2]*Institute for Materials Research, Tohoku University, Sendai 980-8577, Japan*
[3]*WPI Advanced Institute for Materials Research, Tohoku University, Sendai 980-8577, Japan*
[4]*Center for Spintronics Research Network, Tohoku University, Sendai 980-8577, Japan*
[5]*Advanced Science Research Center, Japan Atomic Energy Agency, Tokai 319-1195, Japan*

The spin Seebeck effect (SSE) is observed in magnetic insulator|heavy metal bilayers as an inverse spin Hall effect voltage under a temperature gradient. The SSE can be detected nonlocally as well, viz. in terms of the voltage in a second metallic contact (detector) on the magnetic film, spatially separated from the first contact that is used to apply the temperature bias (injector). Magnon-polarons are hybridized lattice and spin waves in magnetic materials, generated by the magnetoelastic interaction. Kikkawa *et al.* [Phys. Rev. Lett. **117**, 207203 (2016)] interpreted a resonant enhancement of the local SSE in yttrium iron garnet (YIG) as a function of the magnetic field in terms of magnon-polaron formation. Here we report the observation of magnon-polarons in *nonlocal* magnon spin injection/detection devices for various injector-detector spacings and sample temperatures. Unexpectedly, we find that the magnon-polaron resonances can suppress rather than enhance the nonlocal SSE. Using finite element modelling we explain our observations as a competition between the SSE and spin diffusion in YIG. These results give unprecedented insights into the magnon-phonon interaction in a key magnetic material.

I. INTRODUCTION

When sound travels through a magnet the local distortions of the lattice exert torques on the magnetic order due to the magnetoelastic coupling[1]. By reciprocity, spin waves in a magnet affect the lattice dynamics. The coupling between spin and lattice waves (magnons and phonons) has been intensively researched in the last half century[2,3]. Yttrium iron garnet (YIG) has been a singularly useful material here, because it can be grown with exceptional magnetic and acoustic quality[2]. Magnons and phonons hybridize at the (anti)crossing of their dispersion relations, a regime that has attracted recent attention[4–10]. When the quasiparticle lifetime-broadening is smaller than the interaction strength, the strong coupling regime is reached; the resulting fully mixed quasiparticles have been referred to as magnon-polarons[6,7].

In spite of the long history and ubiquity of the magnon-phonon interaction, it still leads to surprises. Evidence of a sizeable magnetoelastic coupling in YIG was recently found in experiments on spin caloritronic effects, i.e. the spin Peltier[11] and spin Seebeck effect[12,13] (SPE and SSE respectively). Recently, Kikkawa *et al.* showed that the hybridization of magnons and phonons can lead to a resonant enhancement of the local SSE in YIG[9]. Bozhko *et al.* found that this hybridization can play a role in the thermalization of parametrically excited magnons using Brillouin light scattering. They observed an accumulation of magnon-polarons in the spectral region near the anticrossing between the magnon and transverse acoustic phonon modes[14]. However, these previous experiments did not address the transport properties of magnon-polarons.

Nonlocal spin injection and detection experiments are of great importance in probing the transport of spin in metals[15], semiconductors[16] and graphene[17]. Varying the distance between the spin injection and detection contacts allows for the accurate determination of the transport properties of the spin information carriers in the channel, such as the spin relaxation length[18]. Recently, it was shown that this kind of experiments are not limited to (semi)conducting materials, but can also be performed on magnetic insulators[19], where the spin information is carried by magnons. Such nonlocal magnon spin transport experiments have provided additional insights in the properties of magnons in YIG, for instance by studying the transport as a function of temperature[20–23] or external magnetic field[24]. Finally, the nonlocal magnon spin injection/detection scheme can play a role in the development of efficient magnon spintronic devices, for example magnon based logic gates[25,26]. In this study, we make use of nonlocal magnon spin injection and detection devices to investigate the transport of magnon-polarons in YIG.

Magnons can be excited magnetically using the oscillating magnetic field generated by a microwave frequency ac current[25], or electrically using a dc current in an adjacent material with a large spin Hall angle, such as platinum[19]. Finally, they can be generated thermally by the SSE[27–30], in which a thermal gradient in the magnetic insulator drives a magnon spin current parallel to the induced heat current.

The generation of magnons via the SSE can be detected in several configurations: First, the heater-induced configuration (hiSSE)[31], which consists of a bilayer YIG|heavy metal sample that is subject to external Peltier elements to apply a temperature gradient nor-
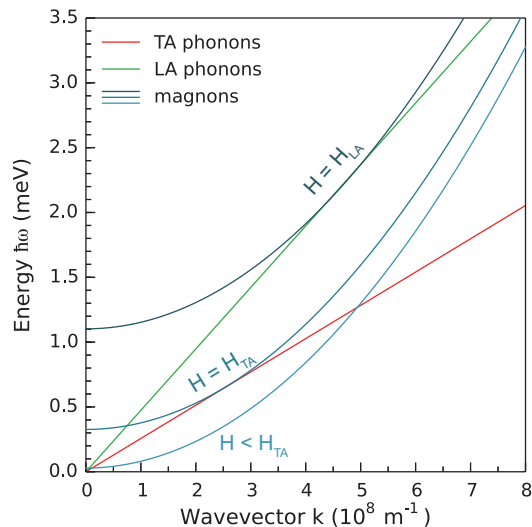
FIG. 1. Dispersion relations for transverse acoustic (TA) phonons, longitudinal acoustic (LA) phonons and magnons, for different values of the applied magnetic field. When the resonance condition is met, i.e. $H = H_{TA}$ or $H = H_{LA}$, magnons hybridize efficiently with TA or LA phonons. Curves are plotted using parameters from Ref. [9].

mal to the plane of the sample. The SSE then generates a voltage across the heavy metal film (explained in more detail below), which can be recorded. Second, the current-induced configuration (ciSSE)[28,32] in which the heavy metal detector used to detect the SSE voltage is simultaneously used as a heater. A current is sent through the heavy metal film, creating a temperature gradient in the YIG due to Joule heating. Due to this temperature gradient, the SSE generates a voltage across the heavy metal film, which can again be recorded. Third, the nonlocal SSE (nlSSE)[19,33], in which a current is sent through a narrow heavy metal strip to generate a thermal gradient via Joule heating as well. However, the SSE signal resulting from this thermal gradient is detected in a second heavy metal strip, located some distance away from the injector.

In the nlSSE, the magnons responsible for generating a signal in the detector strip are generated in the injector vicinity and then diffuse through the magnetic insulator to the detector. The temperature gradient underneath a detector located several microns to tens of microns from the injector does not contribute significantly to the measured voltage[23,34]. In contrast, the hiSSE and ciSSE always have a significant temperature gradient directly underneath the detector. The hiSSE and ciSSE are therefore local SSE configurations, contrary to the nlSSE which is nonlocal.

In all three configurations, the resulting voltage across the heavy metal film is due to magnons which are absorbed at the YIG|detector interface, causing spin-flip scattering of conduction electrons and generating a spin current and spin accumulation in the detector. Due to

the inverse spin Hall effect[35], this spin accumulation is converted into a charge voltage that is measured.

At specific values for the external magnetic field, the phonon dispersion is tangent to that of the magnons and the magnon and phonon modes are strongly coupled over a relatively large region in momentum space (see Fig. 1). At these resonant magnetic field values, the effect of the magnetoelastic coupling is at its strongest and magnon-polarons are formed efficiently. If the acoustic quality of the YIG film is better than the magnetic one (meaning that the phonon lifetime is longer than that of magnons), magnon-polaron formation leads to an enhancement in the hiSSE signal at the resonant magnetic field[9]. This enhancement is attributed to an increase in the effective bulk spin Seebeck coefficient ζ, which governs the generation of magnon spin current by a temperature gradient in the magnet. This was demonstrated experimentally by measuring the spin Seebeck voltage in the hiSSE configuration[9], establishing the role of magnon-polarons in the thermal generation of magnon spin current.

Here we make use of the nlSSE configuration to directly probe not only the generation, but also the transport of magnon-polarons. We show that in the YIG samples under investigation not only ζ, but also the magnon spin conductivity σ_m is resonantly enhanced by the hybridization of magnons and phonons, which leads to signatures in the nonlocal magnon spin transport signals clearly distinct from the hiSSE observations. Notably, resonant features in nonlocal transport experiments have very recently been theoretically predicted by Flebus *et al.*[10], who calculated the influence of magnon-polarons on the YIG transport parameters such as the magnon spin and heat conductivity and the magnon spin diffusion length.

II. EXPERIMENTAL METHODS

A. Sample fabrication

Our nonlocal devices consist of multiple narrow, thin platinum strips (typical dimensions are 100 μm $\times$ 100 nm $\times$ 10 nm [l $\times$ w $\times$ t]) deposited on top of a YIG thin film and separated from each other by a centre-to-centre distance d. We have performed measurements of nonlocal devices on YIG films from Groningen and Sendai, both of which are grown by liquid phase epitaxy on a gadolinium gallium garnet (GGG) substrate in the [111] direction. The YIG film thickness is 210 nm (2.5 μm) for YIG from Groningen (Sendai). The Sendai samples were grown in-house, whereas the Groningen samples were obtained commercially from Matesy GmbH. The saturation magnetization M_S and Gilbert damping constant α are $\mu_0 M_S = 171$ mT and $\alpha = 1.7 \times 10^{-3}$ for the Sendai YIG[36], and $\mu_0 M_S = 180$ mT and $\alpha = 2 \times 10^{-4}$ for the Groningen YIG[19]. In Sendai, four batches of devices where investigated (sample S1 to S4) on pieces cut from the same YIG wafer. The fabrication method and

platinum strip geometry are the same for all batches, but they were not fabricated at the same time, which might lead to variations in for instance the interface quality from batch to batch. In Groningen, two batches of devices where investigated (G1 and G2).

Nonlocal devices fabricated in Groningen are defined in three lithography steps: the first step was used to define Ti/Au markers on top of the YIG film via e-beam evaporation, used to align the subsequent steps. In the second step, Pt injector and detector strips were deposited using magnetron sputtering in an Ar^+ plasma. In the final step, Ti/Au contacts were deposited by e-beam evaporation. Prior to the contact deposition, a brief Ar^+ ion beam etching step was performed to remove any polymer residues from the Pt strip contact areas to ensure optimal electrical contact to the devices. The devices fabricated in Sendai were defined in a single lithography step. Two parallel Pt strips and contact pads were patterned using e-beam lithography followed by a lift-off process, in which 10-nm-thick Pt was deposited using magnetron sputtering in an Ar^+ plasma. Figure 2a shows an optical microscope image of a typical device, with the electrical connections indicated schematically. The central strip functions as a magnon injector while the two outer strips are magnon detectors, measuring the nonlocal signal at different distances from the injector.

B. Electrical measurements

Electrical measurements were carried out in Groningen and in Sendai, using a current-biased lock-in detection scheme. A low frequency ac current of angular frequency ω (typical frequencies are $\omega/(2\pi) < 20$ Hz, and the typical amplitude is $I = 100$ μA_{rms}) is sent through the injector strip, and the voltage on the detector strip is measured at both the frequencies ω (the first harmonic response) and 2ω (the second harmonic response). This allows us to separate processes that are linear in the current, which govern the first harmonic response, from processes that are quadratic in the current which are measured in the second harmonic response[19,28,37]. The signal due to the electrical generation of magnons is therefore detected in the first harmonic, while the signal arising from thermally generated magnons (i.e. the nlSSE) is picked up in the second harmonic.

The measurements in Sendai were carried out in a Quantum Design Physical Properties Measurement System (PPMS), using a superconducting solenoid to apply the external magnetic field (field range up to $\mu_0 H = \pm 10.5$ T). The measurements in Groningen were carried out in a cryostat equipped with a Cryogenics Limited variable temperature insert (VTI) and superconducting solenoid (magnetic field range up to $\mu_0 H = \pm 7.5$ T). Electronic measurements in Groningen are carried out using a home built current source and voltage pre-amplifier (gain 10^4) module galvanically isolated from the rest of the measurement electronics, resulting in a noise level of approximately 3 $nV_{r.m.s.}$ at the output of the lockin amplifier for a time constant of $\tau = 3$ s and a filter slope of 24 dB/octave. The electronic measurements in Sendai were carried out by means of an ac and dc current source (Keithley model 6221) and a lockin amplifier using a time constant of $\tau = 1$ s and a filter slope of 24 dB/octave.

III. EXPERIMENTAL RESULTS

The sample is placed in an external magnetic field H, under an angle $\alpha = 90°$ to the injector/detector strips. The first and second harmonic response of the detector contact, due to electrical and thermal magnon generation in the injector, respectively, are measured simultaneously.

Figure 2b shows the results of two typical nonlocal measurements at different distances, in which $\mu_0 H$ is varied from -3.0 to 3.0 T. Several distinct features can be seen in these results. As the magnetic field is swept through zero, the YIG magnetization and hence the magnon spin polarization change direction, since a magnon always carries a spin opposite to the majority spin in the magnet. This causes a reversal of the polarization of the spin current absorbed by the detector and consequently the voltage V_{nlSSE} changes sign. Additionally, V_{nlSSE} for short distance d (Figure 2b bottom panels) shows an opposite sign compared to V_{nlSSE} for long distance (Figure 2b top panels). This sign-reversal for short distances is a characteristic feature of the nlSSE[19] that has so far been observed to depend on both the thickness of the YIG film t_{YIG} (roughly speaking, at room temperature when $d < t_{YIG}$ the sign will be opposite to that for $d > t_{YIG}$[33]) as well as the sample temperature, where a lower temperature reduces the distance at which the sign-change occurs[21,22].

The sign for short distances corresponds to the sign one obtains when measuring the SSE in its local configurations (hiSSE, indicated schematically in Figure 2c or ciSSE). The results for a hiSSE measurement on sample S3 as a function of H are shown in Figure 2d, and V_{hiSSE} clearly shows the same sign as V_{nlSSE} for short distance. We will discuss the origin of this sign-change in more detail later in this manuscript. The data shown in Figure 2 are from samples with $t_{YIG} = 2.5$ μm, hence the different signs for $d = 2$ μm and $d = 6$ μm. In addition to different signs, the nlSSE vs H curves also show different slopes as the distance changes. This behavior was also observed in thin YIG films[24], where for long distances a strong reduction of the signal was observed which is attributed to the suppression of the magnon spin diffusion length by the magnetic field. For distances below the sign-change distance, the signal shows a relatively steep slope which cannot be due solely to the reduction in the magnon spin diffusion length and is not well understood at the moment.

Resonant features can be observed in the data for $|\mu_0 H| = \mu_0 H_{TA} \approx 2.3$ T, where the subscript TA sig-
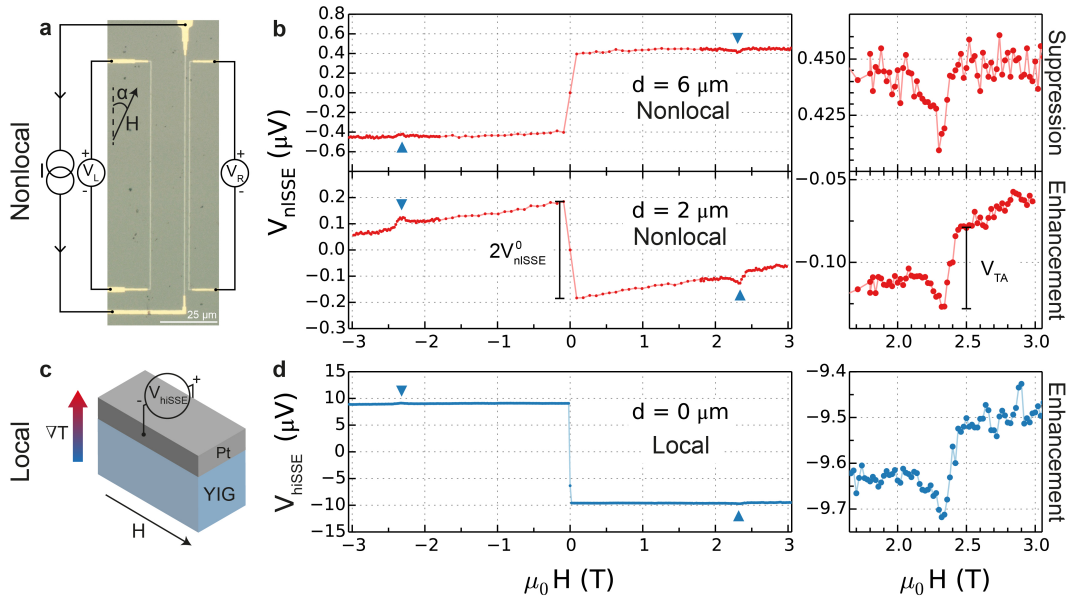
FIG. 2. **a** Microscope image of a typical device, with schematic current and voltage connections. The three parallel lines are the Pt injector/detector strips, connected by Ti/Au contacts. α is the angle between the Pt strips and an applied magnetic field H (in **b-d** $\alpha = 90°$). **b** Nonlocal spin Seebeck (nlSSE) voltage for an injector-detector distance $d = 6$ μm (top) and $d = 2$ μm (bottom) as a function of $\mu_0 H$. At $|\mu_0 H| = \mu_0 H_{\text{TA}} \approx 2.3$ T, a resonant structure is observed that we interpret in terms of magnon-polaron formation (indicated by blue triangles as a guide to the eye). The right column is a close-up of the anomalies for $H > 0$. The results can be summarized by the voltages V_{nlSSE}^0 and V_{TA} as indicated in the lower panels. **c** Schematic geometry of the local heater-induced hiSSE measurements. Here the temperature gradient ∇T is applied by external Peltier elements on the top and bottom of the sample. **d** The hiSSE voltage measured as a function of magnetic field. The close-up around the resonance field (right column) focusses on the magnon-polaron anomaly. All results were obtained at $T = 200$ K. The results for $d = 6$, $d = 2$ and $d = 0$ μm were obtained from sample S1, S2, S3, respectively.

nifies that these features stems from the hybridization of magnons with phonons in the transverse acoustic mode, rather than the longitudinal acoustic mode (LA) which is expected at larger magnetic fields. The rightmost panels of Figure 2 show a close-up of the data around $H = H_{\text{TA}}$. For small d the magnon-phonon hybridization causes a resonant *enhancement* (the absolute value is increased) of V_{nlSSE}, while for large d a resonant *suppression* (the absolute value is reduced) occurs.

Figure 3 shows the results of a magnetic field sweep from sample G1 for both electrically generated magnons (first harmonic) and thermally generated magnons (second harmonic). A feature at $|H| = H_{\text{TA}}$ can be resolved both in the first and second harmonic voltage. This suggests that magnon-phonon hybridization does not only affect the YIG spin Seebeck coefficient, as the first harmonic signal is generated independent of ζ. It indicates that not only the generation, but also the transport of magnons is affected by the hybridization. In the second harmonic, the signal is clearly suppressed at the resonant magnetic field. Unfortunately, because the feature in the first harmonic is barely larger than the noise floor in the measurements (see Fig. 3a and inset), we cannot conclude whether the signal due to electrical magnon generation is enhanced or suppressed at the resonance. Due to the fact that the effect in the first harmonic is so small, in the remainder of this paper we present a systematic study of the effect in the second harmonic, the nlSSE.

As can be seen from Figure 1, the resonant magnetic fields are different for the TA and LA modes (H_{TA} and H_{LA}, respectively). Due to the higher sound velocity in the LA phonon mode, $H_{\text{TA}} < H_{\text{LA}}$, and the resonance due to magnons hybridizing with phonons in this mode can also be observed in our nonlocal experiments. In Appendix A we show the results of a magnetic field scan over an extended field range, and it can be seen that the resonance at H_{LA} also causes a suppression of the nlSSE signal, similar to the H_{TA} resonance. This is comparable to the case for the hiSSE configuration, in which the H_{LA} and H_{TA} resonances both show similar behaviour in the sense that they both *enhance* the hiSSE signal. For the nlSSE case at distances larger than the sign-change distance, both resonances *suppress* the signal.

We now focus on the resonance at H_{TA} in the nlSSE data and carried out nonlocal measurements as a function of magnetic field for various temperatures and distances. Figure 4a (b) shows the distance (temperature) dependent results, obtained from sample S1 (S2). The regions where the sign of the nlSSE equals that of the hiSSE are shaded blue. From Figure 4a the sign-change in V_{nlSSE} can be clearly seen to occur between $d = 2$ and $d = 5$ μm, as at $d = 2$ μm the nlSSE sign is equal to that of the hiSSE for any value of the magnetic field, whereas for $d = 5$ μm it is opposite. Additionally, when comparing
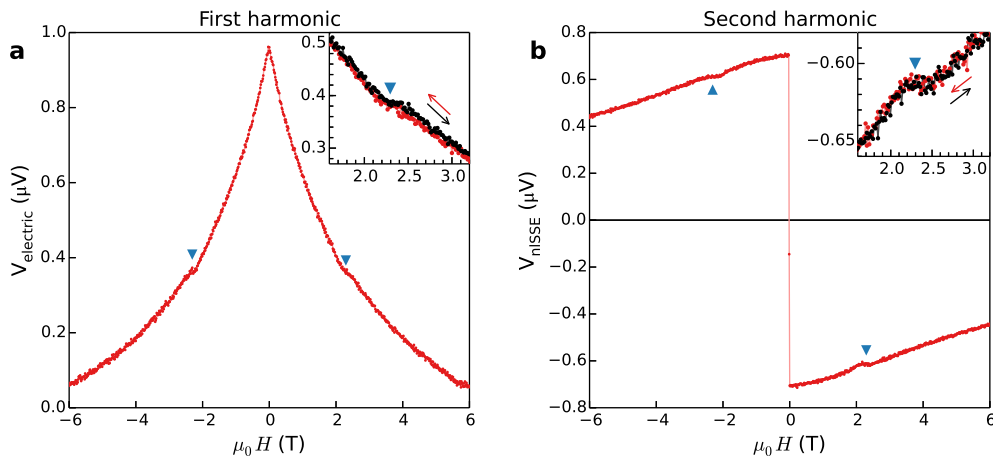
FIG. 3. **a** Nonlocal voltage generated by magnons that are excited electrically (first harmonic response to an oscillating current in the injector contact). An anomaly is observed at $|H| = H_{TA}$ (the field that satisfies the touching condition for magnons and transverse acoustic phonons). The inset shows a second set of data from the same sample, taken with a higher magnetic field resolution ($\mu_0 \Delta H = 15$ mT), sweeping the magnetic field both in the forward (black) and backward (red) directions. **b** nlSSE voltage (second harmonic response) for the same device. V_{nlSSE} is suppressed at $|H| = H_{TA}$. The inset shows the corresponding second harmonic data of the high resolution field sweep. The results were obtained on sample G1 (thickness 210 nm) with $d = 3.5\,\mu\text{m}$ and $I = 150\,\mu\text{A}_{r.m.s.}$, at room temperature. A constant background voltage $V_{bg} = 575$ nV was subtracted from the data in Fig. **a**.

the $V_{nlSSE} - H$ curves for 300 K and 100 K in Figure 4b, the effect of the sample temperature on the sign-change is apparent: At 100 K, the nlSSE sign is opposite to that of the hiSSE over the whole curve. Furthermore, Figure 4b demonstrates the influence of the magnetic field on the sign change, for instance in the curve for $T = 160$ K. At low magnetic fields, the nlSSE sign still agrees with the hiSSE sign (inside the blue shaded region), but around $|\mu_0 H| = 1.5$ T the signal changes sign.

In addition, Figure 4a shows that the role of the magnon-polaron resonance changes as the nlSSE signal undergoes a sign change. For $d \leq 2\,\mu$m, magnon-phonon hybridization enhances V_{nlSSE} at $|H| = H_{TA}$, whereas for $d \geq 5\,\mu$m V_{nlSSE} is suppressed at the resonance magnetic field. Similarly, from Figure 4b we observe that at temperatures $T > 160$ K, magnon-phonon hybridization enhances the nlSSE signal at $|H| = H_{TA}$, while at $T \leq 160$ K the nlSSE is suppressed at H_{TA}. Since the thermally generated magnon spin current is related to the thermal gradient by $\mathbf{j}_m \propto -\zeta \nabla T$, a resonant enhancement in ζ should lead to an enhancement of the nlSSE signal at all distances and temperatures, which is inconsistent with our observations. This is a further indication that not only the generation, but also the transport of magnons is influenced by magnon-polarons.

The temperature dependence of the low-field amplitude of the nlSSE, $V_{nlSSE}^0 = [V(+0.1\text{T}) - V(-0.1\text{T})]/2$, and the magnitude of the resonance, $V_{TA} = V(H_{TA} + 0.2\text{T}) - V(H_{TA})$, (both indicated in Figure 2b) are shown in Figure 5a and 5b respectively. The curve for V_{nlSSE}^0 at $d = 6\,\mu$m agrees well with an earlier reported temperature dependence of the nlSSE at distances which are

larger than the film thickness[23], while that at $d = 2$ μm qualitatively agrees with earlier reports for distances shorter than the YIG film thickness[21,22]. Moreover, from the distance dependence of V_{nlSSE}^0 we have extracted the magnon spin diffusion length λ_m as a function of temperature, which is shown in Appendix B. $\lambda_m(T)$ obtained from the Sendai YIG approximately agrees with that for Groningen YIG[23] for temperatures $T > 30$ K, but differs in the low temperature regime. For further discussion we refer to Appendix B. The temperature dependence of V_{TA} is different from that of V_{nlSSE}^0, since first of all no change in sign occurs here even for $d = 2\,\mu$m and furthermore a clear minimum appears in the curve around $T = 50$ K. This indicates that the resonance has a different origin than the nlSSE signal itself, i.e. magnon-polarons are affected differently by temperature than pure magnons.

The resonant magnetic field H_{TA} decreases with increasing temperature, reducing from $\mu_0 H_{TA} \approx 2.5$ T at 3 K to $\mu_0 H_{TA} \approx 2.2$ T at room temperature as shown in Figure 5c. In earlier work by some of us regarding the magnetic field dependence of the nonlocal magnon transport signal at room temperature, structure in the data at $\mu_0 H = 2.2$ T was indeed observed[24], but not understood at that time. It is now clear that this structure can be attributed to magnon-phonon hybridization. H_{TA} depends on the following three parameters[9]: The YIG saturation magnetization M_s, the spin wave stiffness constant D_{ex} and the TA-phonon sound velocity c_{TA}. D_{ex} is approximately constant for $T < 300$ K[38] and both M_s and c_{TA} decrease with temperature. The reduction of H_{TA} as temperature increases from 3 K to 300 K can be explained by accounting for a 7 % decrease of c_{TA} in
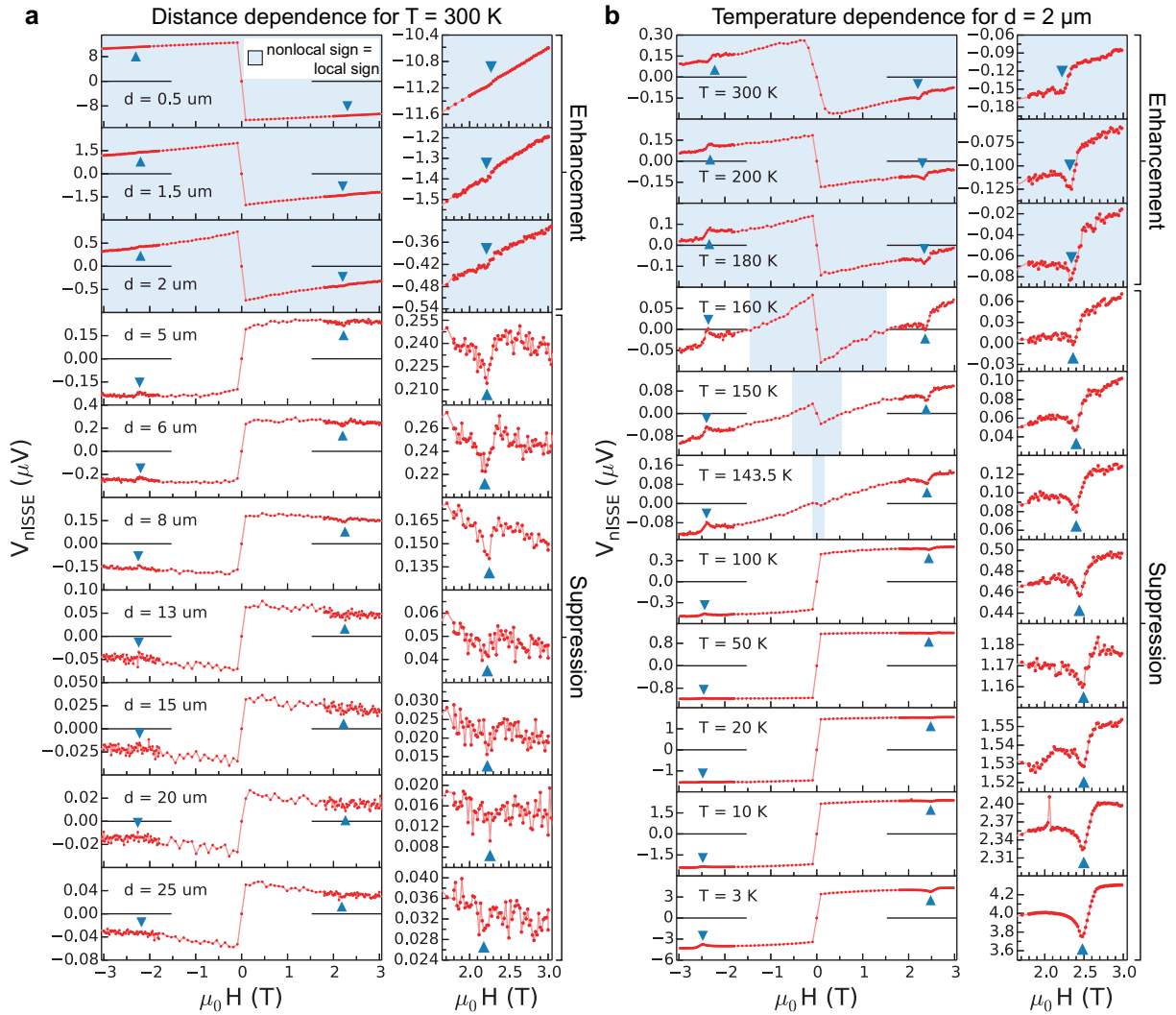
FIG. 4. **a** V_{nlSSE} vs H for various injector-detector separations at $T = 300$ K. **b** V_{nlSSE} vs H for different temperatures and $d = 2$ μm. The data in Figs. **a** and **b** are from sample S1 and S2, respectively, and is the average of a forward and backward magnetic field sweep[a]. The magnon-polaron resonance is indicated by the blue arrows. The blue shading in the graphs indicates the region in which the sign of the nlSSE signal agrees with that of the hiSSE. The right column in both **a** and **b** shows close-ups of the data around the positive resonance field (blue triangles). The data in the close-ups has been antisymmetrized with respect to H, i.e. $V = (V(+H) - V(-H))/2$. Fig. **a** shows that when the contacts are close ($d \leq 2$ μm), the magnon-polaron resonance enhances V_{nlSSE}, while for long distances V_{nlSSE} is suppressed at the resonance magnetic field. For very large distances ($d \geq 20$ μm), the resonance cannot be observed anymore. Similarly in Fig. **b**, for temperatures $T \geq 180$ K, the magnon-polaron resonance enhances the nlSSE signal, while for lower temperatures the nlSSE signal is suppressed. The excitation current $I = 100$ μA$_{r.m.s.}$ for all measurements.

[a] The voltage shown is given by $V_{H+} = (V_{backward}(H) - V_{backward}(-H))/2$ and $V_{H-} = (V_{forward}(H) - V_{forward}(-H))/2$, where V_{H+} is the voltage at postive magnetic field values and V_{H-} that at negative magnetic field values.

the same temperature interval, taking the temperature dependence of M_s into consideration[39]. The results regarding the behaviour of the magnon-polaron resonance qualitatively agree for the Sendai and Groningen YIG (see Appendix C for the temperature dependent results for sample G2).

Moreover, we performed measurements of the nlSSE signal as a function of the injector current, and found that the nlSSE scales linearly with the square of the cur-

rent at high temperatures, as expected. However, at low temperatures ($T < 10$ K) and sufficiently high currents (typically, $I > 50$ μA), this linear scaling breaks down (see Appendix D). This could be a consequence of the strong temperature dependence of the YIG and GGG heat conductivity at these temperatures[40,41]. The injector heating causes a small increase in the average sample temperature which increases the heat conductivities of the YIG and GGG, thereby driving the system out of
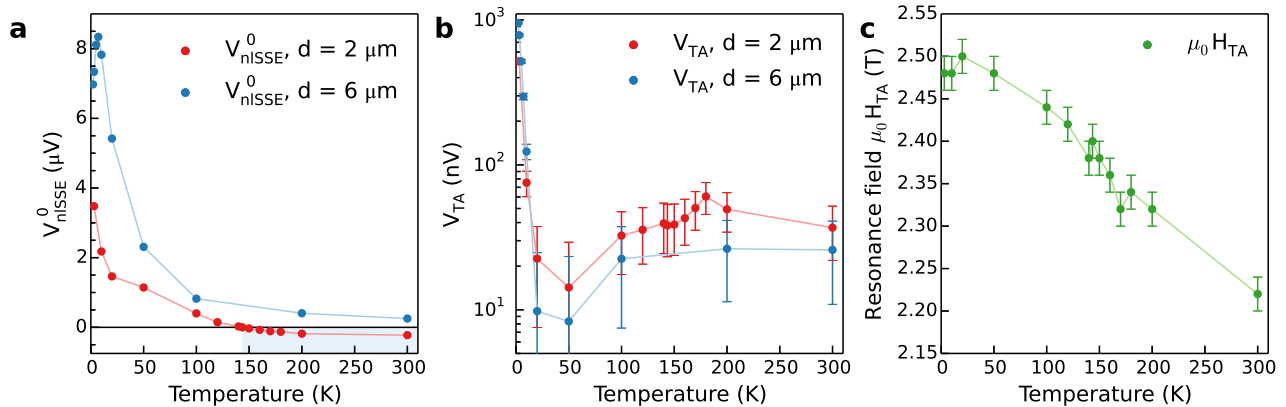
FIG. 5. **a** Temperature dependence of the low-field V_{nlSSE}^0, for $d = 2$ μm and $d = 6$ μm. For 2 μm, the signal changes sign around $T = 143$ K. The blue shading in the graph indicates the regime in which the sign agrees with that of the hiSSE. **b** Temperature dependence of the magnon-polaron resonance V_{TA}. Here, no sign change but a minimum around $T = 50$ K is observed, which is absent in Figure **a**. **c** Temperature dependence of the resonance field H_{TA}. The maximum around $T = 25$ K is likely an artifact resulting from our measurement uncertainty, since it falls within the errorbars and no such maximum was observed for the hiSSE measurements[9]. Error bars in **b** and **c** reflect the peak-to-peak noise in the data used to extract V_{TA} and the step size in the magnetic field scans ($\mu_0 \Delta H = 20$ mT), respectively.

the linear regime. However, it might also be related to the bottleneck effect which is observed in parametrically excited YIG[14]. A more detailed investigation is needed in order to establish the origin of the nonlinearity.

Finally, we have investigated the ciSSE configuration, meaning that current heating of the Pt injector is used to drive the SSE and the (local) voltage across the injector is measured. The sign of the ciSSE voltage corresponds to that obtained in the hiSSE configuration. However, no resonant features were observed in the ciSSE measurements, contrary to the hiSSE and nlSSE configurations. We believe that this is due to the low signal-to-noise ratio in the ciSSE configuration, which could cause the feature to be smaller than the noise level in our ciSSE measurements. We refer to Appendix E for further discussion.

IV. MODELLING

The physical picture underlying the thermal generation of magnons has been a subject of debate in the magnon spintronics field recently. Previous theories explain the SSE as being due to thermal spin pumping, caused by a temperature difference between magnons in the YIG and electrons in the platinum[13,42,43]. However, the recent observations of nonlocal magnon spin transport and the nlSSE give evidence that not only the interface but also the bulk magnet actively contributes and even dominates the spin current generation. At elevated temperatures the energy relaxation should be much more efficient than the spin relaxation, which implies that the magnon chemical potential (and its gradient) is more important as a non-equilibrium parameter than the temperature difference between magnons and phonons. A

model for thermal generation of magnon spin currents based on the bulk SSE[44] which takes into account a non-zero magnon chemical potential has been proposed in order to explain the observations[34]. We make use of a finite element techinque to apply this model to our specific device geometry. The finite element implementation is described concisely in the next section, and in great detail in our previous work[33,34].

A. Finite element model

The two-dimensional finite element model (FEM) is implemented in COMSOL MultiPhysics (v4.4). The linear response relation of heat and spin transport in the bulk of a magnetic insulator reads

$$\begin{pmatrix} \frac{2e}{\hbar}\mathbf{j}_m \\ \mathbf{j}_Q \end{pmatrix} = -\begin{pmatrix} \sigma_m & \zeta/T \\ \hbar\zeta/2e & \kappa \end{pmatrix} \begin{pmatrix} \boldsymbol{\nabla}\mu_m \\ \boldsymbol{\nabla}T \end{pmatrix}, \qquad (1)$$

where $\mathbf{j}_m$ is the magnon spin current, $\mathbf{j}_Q$ the total (magnon and phonon) heat current, μ_m the magnon chemical potential, T the temperature (assumed to be the same for magnons and phonons by efficient thermalization), σ_m the magnon spin conductivity, κ the total (magnon and phonon) heat conductivity and ζ the spin Seebeck coefficient. We disregard temperature differences arising from the Kapitza resistances at the Pt|YIG or YIG|GGG interfaces. $-e$ is the electron charge and $\hbar$ the reduced Planck constant. The diffusion equations for spin and heat read

$$\nabla^2 \mu_m = \frac{\mu_m}{\lambda_m^2}, \qquad (2)$$

$$\nabla^2 T = \frac{j_c^2}{\kappa\sigma}, \qquad (3)$$

where j_c is the charge current density in the injector contact, σ and κ the electrical and thermal conductivity and λ_m the magnon spin diffusion length. Eq. (3) represents the Joule heating in the injector that drives the SSE.

In the simulations, $t_{\mathrm{YIG}} = 2.5\ \mu\mathrm{m}$ and $w_{\mathrm{YIG}} = 500\ \mu\mathrm{m}$ are the thickness and width of the YIG film, on top of a GGG substrate that is 500 μm thick. w_{YIG} is much larger than λ_m and finite size effects are absent. The injector has a thickness of $t_{\mathrm{Pt}} = 10$ nm and a width of $w_{\mathrm{Pt}} = 300$ nm. The spin and heat currents normal to the YIG|vacuum, Pt|vacuum and GGG|vacuum interfaces vanish. At the bottom of the GGG substrate the boundary condition $T = T_0$ is used, i.e. the bottom of the sample is taken to be thermally anchored to the sample probe. Furthermore, there is no flow of spin current into the GGG. This assumption should hold at room temperature but likely not at low temperatures, since the existence of a paramagnetic spin Seebeck effect[45] indicates that GGG under strong magnetic fields can sustain spin excitations at low temperature. The spin current across the Pt|YIG interface is given by $j_m^{\mathrm{int}} = g_s\,(\mu_s - \mu_m)$, where g_s is the effective spin conductance of the interface, μ_s is the spin accumulation on the metal side of the interface and μ_m is the magnon chemical potential on the YIG side of the interface. The nonlocal voltage is then found by calculating the average spin current density $\langle j_s \rangle$ flowing in the detector, which is then converted to non-local voltage using $V_{\mathrm{nlSSE}} = \theta_{\mathrm{SH}} L \langle j_s \rangle / \sigma$, where θ_{SH} is the spin Hall angle in platinum and L is the length of the detector strip. The spin current in the platinum contact relaxes over the characteristic spin relaxation length λ_s.

The parameters used for platinum in the model are $\theta_{\mathrm{SH}} = 0.11$, $\sigma = 1.9 \times 10^6$ S/m, $\lambda_s = 1.5$ nm and $\kappa = 26$ W/(m K). For YIG, $\sigma_m = 3.7 \times 10^5$ S/m, $\lambda_m = 9.4\ \mu\mathrm{m}$ which was obtained in our previous work[23]. Furthermore, $\kappa = 7$ W/(m K), based on YIG thermal conductivity data from Ref. 41. For the bulk spin Seebeck coefficient at zero field we use $\zeta^0 = 500$ A/m, based on our previous work in which we gave an estimate for ζ at room temperature[33]. For GGG, the spin conductivity and spin Seebeck coefficient are set to zero. For the GGG thermal conductivity we use $\kappa = 9$ W/(m K), based on data from Refs. 40 and 46. Finally, for the effective spin conductance of the interface we have $g_s = 3.4 \times 10^{11}$ S/m^2. This is roughly a factor 30 smaller than in our earlier work[23]. In the next section we discuss the reason for this smaller g_s further.

B. Model results

This model has been reasonably successful in explaining the nonlocal signals (due to both thermal and electrical generation) in the long distance limit[23,33], yet is not fully consistent with experiments in the short distance limit for thermally generated magnons[33]. The physical picture captured by the model is explained in Figure 6a and b, where for this study we focus on the thermally

generated magnons driving the nlSSE. In Figure 6a a schematic side-view of the YIG|GGG sample with a platinum injector strip on top is shown. A current is passed through the injector, causing it to heat up to temperature T_H. The bottom of the GGG substrate is thermally anchored at T_0. As a consequence of Joule heating, a thermal gradient arises in the YIG, driving a magnon current $\mathbf{J}_Q^m = -\zeta/T \boldsymbol{\nabla} T$ parallel to the heat current, i.e. radially away from the injector. This reduces the number of magnons in the region directly below the injector (magnon depletion).

In Figure 6b the same schematic cross-section is shown, but now the colour coding refers to the magnon chemical potential μ_m. Directly below the injector contact μ_m is negative due to the magnon depletion in this region (μ^-). At the YIG|GGG interface, magnons accumulate since they are driven towards this interface by the SSE but are reflected by the GGG, causing a positive magnon chemical potential μ^+ to build up. Note that the μ^- and μ^+ regions are not equal in size since part of the magnon depletion is replenished by the injector contact, which acts as a spin sink. Due to the gradient in magnon chemical potential, a diffuse magnon spin current J_d^m now arises in the YIG given by $\mathbf{J}_d^m = -\sigma_m \boldsymbol{\nabla} \mu_m$.

The combination of these two processes leads to a typical magnon chemical potential profile as shown in Figure 6c, which is obtained from the FEM at room temperature. The sign change from μ^- to μ^+ occurs at a distance of roughly $d_{sc} = 2.6\ \mu\mathrm{m}$ from the injector, comparable to the YIG film thickness.

The effective spin conductance of the Pt|YIG interface g_s was used as a free parameter in order to get approximate agreement between the modelled and experimentally observed sign-change distance d_{sc}. The value for g_s is approximately a factor 30 lower than what we estimated from theory[34] and used in our previous work[23] to model the distance dependence of the *electrically* generated magnon spin signal. When using $g_s = 9.6 \times 10^{12}$ S/m^2 (the same as in Refs. 23 and 34) to model the *thermally* generated signal, $d_{sc} \approx 300$ nm (for $t_{\mathrm{YIG}} = 2.5\ \mu\mathrm{m}$) which is much shorter than what we observe in the experiments. This discrepancy arises for both the Groningen and Sendai samples.

Taking all processes into account, it should be possible to describe electrical and thermal generation of magnons with the same g_s. The discrepancy between models for electrically and thermally generated magnon transport might indicate that some of the material parameters such as spin or heat conductivity and spin diffusion length (for both YIG and platinum) we used are not fully accurate. However, it could also indicate the presence of physical processes that are not accounted for in the modelling. This would mean that the model needs to be refined further, for instance by including temperature differences at material interfaces which are currently neglected, and the interfacial spin Seebeck and spin Peltier contributions.

The value of d_{sc} depends mainly on four parameters: The thickness of the YIG film t_{YIG}, the transparency
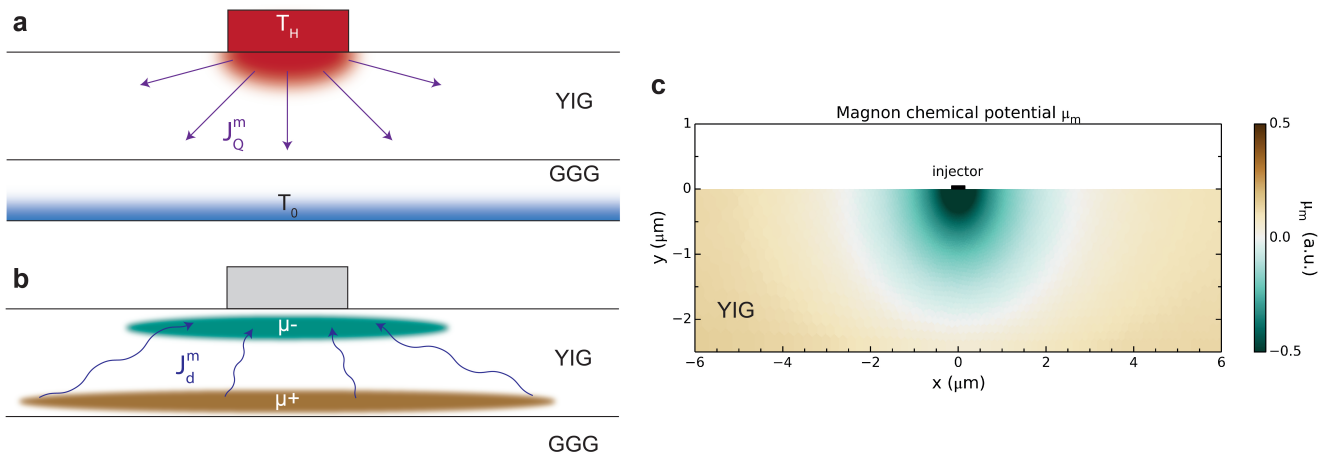
FIG. 6. **a** Sketch of the Joule heating in the injector, heating it up to temperature T_H. This leads to a thermal gradient in the YIG. The bulk SSE generates a magnon current J_Q^m antiparallel to the local temperature gradient, spreading into the film away from the contact. When the spin conductance of the contact is sufficiently small, this leads to a depletion of magnons below the injector, indicated in Figure **b** as μ^-. When the magnons are reflected at the GGG interface, J_Q^m accumulates magnons at the YIG|GGG interface, shown in Figure **b** as μ^+. The chemical potential gradient induces a backward and sideward diffuse magnon current J_d^m. Both processes in Figure **a** and **b** are included in the finite element model (FEM). Its results are plotted in Figure **c** in terms of a typical magnon chemical potential profile. μ_m changes sign at some distance from the injector, also at the YIG surface, where it can be detected by a second contact. The magnon-polaron resonance enhances both the spin Seebeck coefficient ζ and the magnon spin conductivity σ_m. The increased backflow of magnons to the injector causes a suppression of the nonlocal signal at long distances (see Figure 6).

of the platinum|YIG injector interface, parameterized in the effective spin conductance g_s, the magnon spin conductivity of the YIG σ_m and finally the magnon spin diffusion length λ_m. At high temperatures (i.e. close to room temperature), the thermal conductivities κ_{GGG} and κ_{YIG} are similar in magnitude[46] and affect d_{sc} only weakly, allowing us to focus here on the spin transport.

Increasing t_{YIG} or σ_m increases d_{sc} since this reduces the spin resistance of the YIG film, allowing the depleted region to spread further throughout the YIG. However, increasing g_s or λ_m causes the opposite effect and reduces d_{sc} since this increases the amount of μ^- which is absorbed by the injector contact compared to that which relaxes in the YIG. The precise dependency of d_{sc} on these parameters is nontrivial but can be explored using our finite element model. Ganzhorn *et al.* and Zhou *et al.* in Refs. 21 and 22 observed that d_{sc} becomes smaller with lower temperatures. This indicates that the ratio of the effective spin resistance of YIG to that of the Pt contact increases, causing spins to relax preferentially into the contact and thereby reducing the extend of μ^-.

Flebus *et al.* developed a Boltzmann transport theory for magnon-polaron spin and heat transport in magnetic insulators[10]. Here we implement the salient features of magnon-polarons into our finite element model. We observe that when the combination of g_s, λ_m, σ_m, t_{YIG} and d is such that the detector is probing the depletion region, i.e. μ^-, the magnon-polaron resonance causes enhancement of the nlSSE signal. Conversely, when the detector is probing μ^+ the resonance causes a suppres-

sion of the signal. This cannot be explained by assuming that the only effect of the magnon-polaron resonance is the enhancement of ζ, as this would simply increase the thermally driven magnon spin current J_Q^m and hence enhance both μ^- and μ^+. To understand this behaviour, we have to account for the enhancement of σ_m by the magnon-polaron resonance as well.

A resonant increase in σ_m leads to an increased diffusive backflow current J_d^m, which can lead to a reduction of the magnon spin current reaching the detector at large distances. We model the effect of the magnon-phonon hybridization by assuming a field-dependent magnon spin conductivity $\sigma_m(H)$ and bulk spin Seebeck coefficient $\zeta(H)$, which are both enhanced at the resonant field H_{TA}. Note that the field-dependence only includes the contribution from the magnon-polarons[10], and does not include the effect of magnons being frozen out by the magnetic field[24,47–49] since this is not the focus of this study. The model is used to calculate the spin current flowing into the detector contact as a function of magnetic field, from which we calculate the voltage drop over the detector due to the inverse spin Hall effect. We then vary the ratios of enhancement for σ_m and ζ, i.e. $f_\sigma = \sigma_m(H_{TA})/\sigma_m^0$ and $f_\zeta = \zeta(H_{TA})/\zeta^0$, where σ_m^0 and ζ^0 are the zero field magnon spin conductivity and spin Seebeck coefficient and $\sigma_m(H_{TA})$, $\zeta(H_{TA})$ are these parameters at the resonant field. The ratio of enhancement $\delta = f_\zeta/f_\sigma$ is crucial in obtaining agreement between the experimental and modelled data. To change delta, we fix $f_\zeta = 1.09$ and vary f_σ. The value for f_ζ is comparable to the enhance-

ment in ζ calculated from theory for low temperatures[10].

V. COMPARISON BETWEEN MODEL AND EXPERIMENT

Figure 7 shows a comparison between the distance dependence of V_{nlSSE}^0 and V_{TA} obtained from experiments (Fig. 7a) and the finite element model (Fig. 7b and c) at room temperature. In Figure 7a, V_{nlSSE}^0 shows a change in sign around $d = 4\,\mu\mathrm{m}$, while V_{TA} has a positive sign over the whole distance range. Fig. 7b shows the model results for V_{nlSSE}^0 (red), and the voltage measured at $H = H_{\mathrm{TA}}$ for $\delta = 2$ (green) and $\delta = 0.5$ (purple). While the voltage obtained from the model is approximately one order of magnitude lower than in experiments, the qualitative behaviour of the experimental data is reproduced. In particular, the modelled d_{sc} approximately agrees with the experimentally observed distance.

For $\delta = 2$, the modelled voltage at H_{TA} is always enhanced with respect to V_{nlSSE}^0 (for $d < d_{sc}$, $V(H_{\mathrm{TA}}) < V_{\mathrm{nlSSE}}^0$ and for $d > d_{sc}$, $V(H_{\mathrm{TA}}) > V_{\mathrm{nlSSE}}^0$). This is not consistent with the experiments as it leads to a sign change in V_{TA}, which is defined as $V_{\mathrm{TA}} = V_{\mathrm{nlSSE}}^0 - V(H_{\mathrm{TA}})$, as can be seen from Fig. 7c.

However, for $\delta = 0.5$, $V(H_{\mathrm{TA}})$ is enhanced with respect to V_{nlSSE}^0 for $d < d_{sc}$ but suppressed for $d > d_{sc}$. This results in a positive sign for V_{TA} over the full distance range, comparable to the experimental observations. The full magnetic field dependence obtained from the model can be found in Appendix F. As can be seen from the inset in Fig. 7c, $\delta = 0.5$ results in a decay of V_{TA} with distance which is comparable to the experimentally observed $V_{\mathrm{TA}}(d)$ (inset Fig. 7a). We fitted the data for V_{TA} obtained from both the experiments and the simulations to $V_{\mathrm{TA}}(d) = A \exp{-d/\ell_{\mathrm{TA}}}$, where A is the amplitude and ℓ_{TA} the length scale over which V_{TA} decays. From the fits, we obtain $\ell_{\mathrm{TA}}^{\mathrm{exp}} = 6.3 \pm 1.2\,\mu\mathrm{m}$ and $\ell_{\mathrm{TA}}^{\mathrm{sim}} = 10.6 \pm 0.1$ $\mu\mathrm{m}$ at room temperature, where we have fitted to the model results for $\delta = 0.5$. From the simulations, we find that ℓ_{TA} is influenced by the value used for δ, where a smaller δ leads to a longer ℓ_{TA}. This could indicate that δ has to be increased slightly to obtain better agreement between $\ell_{\mathrm{TA}}^{\mathrm{exp}}$ and $\ell_{\mathrm{TA}}^{\mathrm{sim}}$.

Therefore, in order to explain the observations, $0.5 < \delta < 1$, i.e. the relative enhancement due to magnon-phonon hybridization in σ_m has to be larger than that of ζ. $\ell_{\mathrm{TA}}^{\mathrm{exp}}$ is enhanced at low temperatures (see Appendix B for the distance dependence of V_{TA} at low temperatures). This could indicate that δ decreases with decreasing temperatures. For further discussion we refer to Appendix B.

The model results depend sensitively on g_s. A larger g_s reduces the d_{sc} observed in the model, so that our model no longer qualitatively fits the distance dependence of V_{nlSSE} obtained in experiments. As a consequence, the δ needed to model the resonant suppression of the signal at H_{TA} for long distances decreases further, which would imply that the enhancement in σ_m is much stronger than

that in ζ. Such a strong enhancement in σ_m should result in a clear magnon-polaron resonance in the electrically generated magnon spin signal, whereas we observed only a small effect here (see Fig. 3a). This is an indication that our choice of reducing g_s compared to our previous work is justified.

VI. DISCUSSION

We report resonant features in the nlSSE as a function of magnetic field, which we ascribe to the hybridization of magnons and acoustic phonons. They occur at magnetic fields that obey the "touch" condition at which the magnon frequency and group velocity agree with that of the TA and LA phonons. The signals are enhanced (peaks) for short injector-detector distances and high temperatures, but suppressed (dips) for long distances and/or low temperatures. The temperature dependence of the TA resonance differs from that of the low-field nlSSE voltage, indicating that different physical mechanisms are involved (this in contrast to the local SSE configuration). The sign of the nlSSE signal corresponds to that of the signal in the hiSSE configuration for distances below the sign-change distance. In this regime the magnon-polaron feature causes signal enhancement, similar to the hiSSE configuration. For distances longer than the sign-change distance, the nlSSE signal is suppressed at the resonance magnetic field.

These results are consistent with a model in which transport is diffuse and carried by strongly coupled magnons and phonons[10] (magnon-polarons). Theory predicts an enhancement of all transport coefficients when the acoustic quality of the crystal is better than the magnetic one. Simulations show that the dip observed in the nlSSE is not caused by deteriorated acoustics, but by a competition between the thermally generated, SSE driven magnon current and the diffuse backflow magnon current which are both enhanced at the resonance. More experiments including thermal transport as well as an extension of the Boltzmann treatment presented in Ref. 10 to 2D geometries are necessary to fully come to grips with heat and spin transport in YIG.

Additionally, we observed features in the electrically generated magnon spin signal at the resonance magnetic field. This is further evidence that not only the generation of magnons via the SSE, but additional transport parameters such as the magnon spin conductivity are affected by magnon-polarons.

The nonlocal measurement scheme provides an excellent platform to study magnon transport phenomena and opens up new avenues for studying the magnetoelastic coupling in magnetic insulators. Finally, these results are an important step towards a complete physical picture of magnon transport in magnetic insulators in its many aspects, which is crucial for developing efficient magnonic devices.
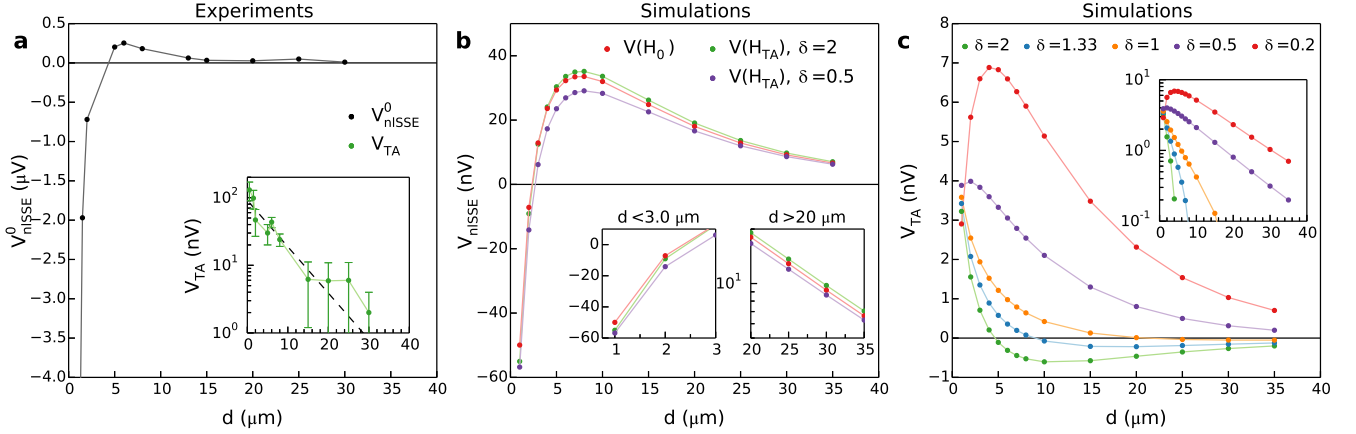
FIG. 7. **a** Distance dependence of V^0_{nlSSE} and V_{TA} (inset) measured at room temperature. The dashed line in the inset is an exponential fit to the data. V^0_{nlSSE} changes sign around $d = 4\,\mu$m, while V_{TA} remains positive. **b** Calculated distance dependence of V_{nlSSE} at zero magnetic field (red, this corresponds to V^0_{nlSSE}) and at the resonant field for $\delta = 2$ (green) and $\delta = 0.5$ (purple). Here δ is a parameter that measures the relative enhancement of the spin Seebeck coefficient compared to the magnon spin conductivity, as explained in the main text. Insets shows the signal decay at long distances ($d \geq 20\,\mu$m) on a logarithmic scale, and for short distances ($d \leq 3\,\mu$m) on a linear scale. **c** Modelled distance dependence of V_{TA} for various values of δ on a linear scale (inset for logarithmic scale). $\delta = 0.5$ results in a positive sign for V_{TA} over the full distance range with a slope that roughly agrees with experiments (cf. insets of Figure **a** and **c**). Reducing δ further leads to a more gradual slope for V_{TA}. In the simulations, the SSE enhancement is $f_\zeta = 1.09$, while f_σ is varied with δ.

VII. ACKNOWLEDGEMENTS

Appendix A: Resonances at H_{TA} and H_{LA}

Figure 8 shows the results of a magnetic field sweep over an extended range ($\mu_0 H = -10$ to $+10$ T) at $T = 20$ K. Resonances stemming from the hybridization of magnons with phonons in the TA and LA mode can be seen in the data, at $\mu_0 H = \mu_0 H_{\text{TA}} \approx 2.5$ T and $\mu_0 H = \mu_0 H_{\text{LA}} \approx 9.2$ T, respectively.
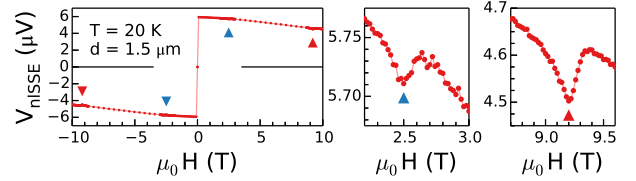
FIG. 8. nlSSE measurements over an extended magnetic field range. In addition to the resonant suppression of V_{nlSSE} at H_{TA}, a second resonance due to the hybridization of magnons with phonons in the longitudinal acoustic mode can be seen in the data at higher magnetic field amplitude. The smaller panels show a close-up of the data around $H = H_{\text{TA}}$ and $H = H_{\text{LA}}$. Data obtained from sample S1.

Appendix B: Distance and temperature dependence of V^0_{nlSSE}, V_{TA} and λ_m

Typical low-temperature magnetic field sweeps for different distances are shown in Fig. 9, for $T = 10$ K. At this temperature, the resonance can be very clearly seen for all distances. We performed such series of measurements at several temperatures, and extracted V^0_{nlSSE} and V_{TA} from each measurement. Figure 10a shows the distance dependence of V^0_{nlSSE} for various temperatures, displaying only the data from devices with $d > 5$ μm (i.e. well beyond d_{sc}). Solid lines in the figure are fits to the experssion $V^0_{\text{nlSSE}}(d) = C_1 \exp(-d/\lambda_m)$, with C_1 a constant which parameterizes the magnon generation and detection efficiency and λ_m the magnon spin diffusion length. Figure 10b shows the temperature dependence of λ_m ob-
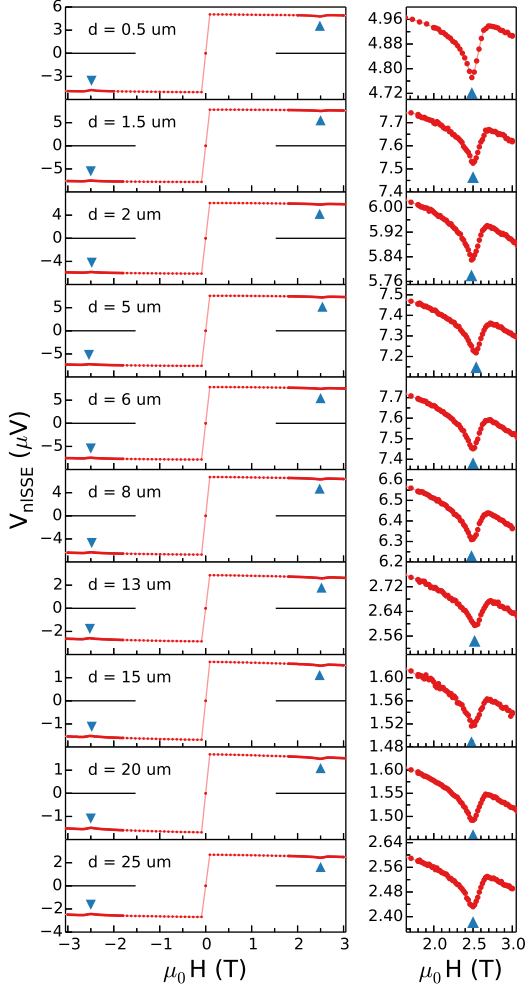
FIG. 9. Low temperature distance dependence of V_{nlSSE} as a function of magnetic field. Data obtained at $T = 10$ K from sample S1.

FIG. 10. **a** Distance dependence of V_{nlSSE}^0 on a logarithmic scale. Solid lines are fits to the expression $V_{\text{nlSSE}}^0 = C_1 \exp -d/\lambda_m$. **b** Magnon spin diffusion lengths $\lambda_m(T)$ extracted from the fits in **a**. **c** Distance dependence of V_{TA} at low temperatures. Solid lines are again exponential fits to the data. Data obtained from samples S2 and S4.

tained from the fits. $\lambda_m(T)$ found here approximately agrees with previous results obtained in Groningen[23], the main difference being the observed enhancement of λ_m to beyond its room temperature value for $T \leq 10$ K. In Ref. 23, YIG samples with a film thickness of 210 nm where studied and the trend of $\lambda_m(T)$ is approximately the same as what we report here but does not show an enhancement at low temperatures. The difference in temperature dependence of λ_m between thick (2.5 μm) and thin (210 nm) YIG films might hint at the existence of a spin-sink effect of the GGG substrate at low temperatures. Since Wu *et al.* showed[45] that GGG can act as a spin current source under the influence of a thermal gradient, it is expected that it can also sink spin currents in the absence of a thermal gradient in the GGG. This could lead to a leakage of magnon spin current out of the YIG film and hence an additional relaxation channel for the magnons. In a thin YIG sample, the influence of the

GGG will be larger than for a thicker sample which could explain the difference in λ_m between very thin films[23], films of intermediate thickness which we discuss here and the much longer diffusion lengths found in bulk YIG at low temperatures by Giles *et al.*[50].

Figure 10c shows the distance dependence of V_{TA} at low temperatures. Interestingly, V_{TA} decays much slower than V_{nlSSE}^0 at these temperatures (cf. Fig. 10a and Fig. 10c). This is different from the room temperature case presented in Fig. 7, where V_{TA} and V_{nlSSE}^0 show a comparable decay length. The solid lines in Fig. 10c are exponential fits to the data from which we obtain ℓ_{TA}, the characteristic length scale over which V_{TA} decays. We find $\ell_{\text{TA}} = 195 \pm 49$ μm at $T = 3$ K, and comparably long lengths for $T = 20$ and 10 K. The precise values should not be taken seriously due to the large error in the fits, and the fact that we are only probing distances much shorter than ℓ_{TA} which makes the uncertainty in the estimation of ℓ_{TA} very large. However, these large values of ℓ_{TA} do show the enhanced decay length of the magnon-polaron resonance at low temperatures. From the FEM, we find that decreasing δ increases the length scale ℓ_{TA}, which could indicate that δ decreases as the temperature drops. The enhanced ℓ_{TA} at low temperatures could also be related to the strongly enhanced phononic mean free path in YIG at low temperatures[41], compared to room temperature. Since the magnon-polarons are composite quasiparticles, an enhanced mean free path for their

phonic constituents could explain their enhancement in decay length compared to ordinary magnons.

Appendix C: Nonlocal spin Seebeck effect in Groningen YIG
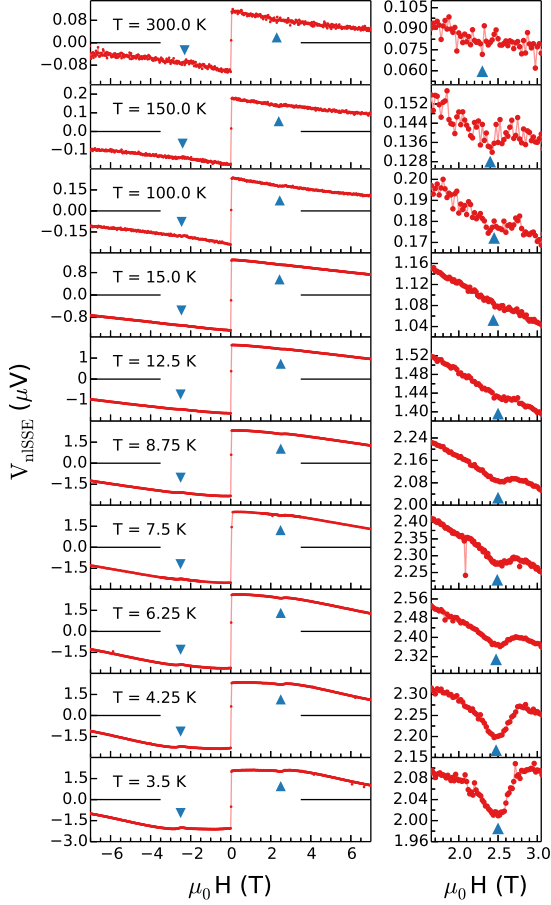
FIG. 11. V_{nlSSE} as a function of magnetic field for various temperatures, as measured on the Groningen YIG sample G2. The injector-detector separation distance was $d = 6.5$ μm.

Figure 11 shows measurement data from the Groningen YIG sample G2 for a device with $d = 6.5$ μm, using the same measurement conventions as depicted in Fig. 2. The magnon-polaron resonance occurs at approximately the same magnetic field as in the Sendai YIG samples. The resonance peak is less sharp in the Groningen YIG. However, the qualitative behavior of the resonance is the same in the Sendai and Groningen YIG. Given the thickness of the YIG film for sample G2 (210 nm) and the injector-detector separation, we are in the limit where $\mathrm{sign}\,(V_{\mathrm{nlSSE}}) \neq \mathrm{sign}\,(V_{\mathrm{hiSSE}})$. Consequently, the magnon-polaron resonance causes suppression of the nlSSE signal. In addition, the temperature dependence of the magnitude of the resonance $(V_{\mathrm{TA}}(T))$ is comparable for YIG from Sendai and from Groningen.

Appendix D: Nonlinearity of V_{nlSSE}^0 and V_{TA} at low temperatures

Figure 12 shows the current dependence of the nlSSE signal and the magnon-polaron resonance dip at $T = 3$ K and $T = 10$ K. The nonlinear behavior of V_{nlSSE}^0 and V_{TA} can be seen from Figs. 12a and 12c, where the current dependence is no longer linear for currents $I_{\mathrm{rms}} > 50$ μA. At $T = 10$ K, both V_{nlSSE}^0 and V_{TA} scale approximately linear with the current squared. A more detailed investigation is needed in order to establish the origin of the nonlinearity.
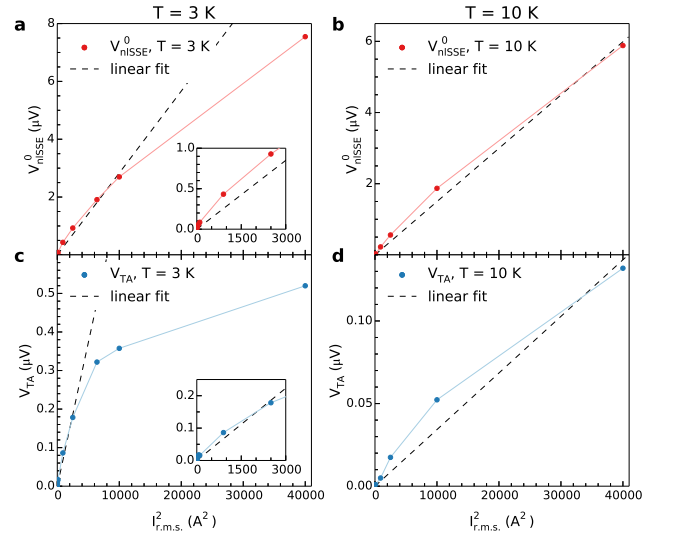
FIG. 12. Nonlinearity of V_{nlSSE}^0 and V_{TA} at low temperatures. Figs. **a** and **c** show the current dependence of V_{nlSSE}^0 and V_{TA} for $T = 3$ K, plotted here vs I_{rms}^2. The dashed line is a linear fit to the data. Inset shows a close-up of the data in the low-current regime ($I < 50$ μA). Figs. **b** and **d** show the same current dependencies but now for $T = 10$ K. Data obtained from sample S3.

Appendix E: Absence of the magnon-polaron resonance in the current induced spin Seebeck effect

Figure 13 shows the result of a measurement in the local, current induced spin Seebeck configuration (ciSSE). In this configuration, the injector is simultaneously used as a detector, i.e. the current is applied to the same strip over which the voltage is measured. The sign of the signal in this configuration matches that of the hiSSE configuration. Interestingly, no resonant features are observed in this configuration, contrary to the hiSSE and nlSSE configurations.
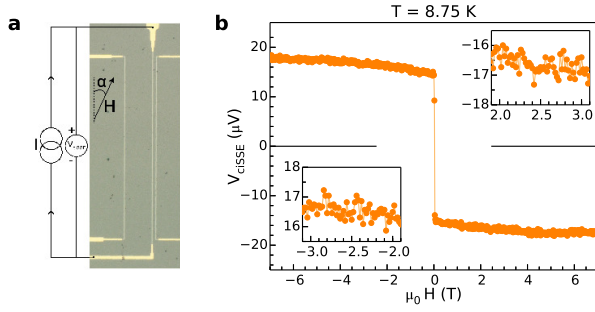
FIG. 13. **a** Measurement configuration for the ciSSE configuration. Current and voltage leads are connected to the same strip. **b** Measurement results for the second harmonic voltage as a function of the magnetic field. The angle $\alpha = 90°$. Insets show close-ups of the data in the regions where the magnon-polaron resonance is expected, i.e. around $|H| = H_{TA}$. However, no resonant features are observed in the data. Measurement was performed at $T = 8.75$ K, and a constant background voltage $V_{off} = 226$ μV was subtracted from the data. Data was obtained from sample G2.

This might be due to the fact that the signal to noise ratio in the ciSSE configuration is typically smaller than in the hiSSE or nlSSE configuration. In the data in

Fig. 13b, $V_{ciSSE}^0 = 14.6$ μV while the r.m.s. noise level is approximately $V_{rms} \approx 228$ nV, which translates in a peak-to-peak noise of $V_{pp} \approx 1.1$ μV. This signal-to-noise ratio is much lower compared to the hiSSE data in Fig. 2d, which shows $V_{hiSSE}^0 = 9.6$ μV at a noise level of $V_{rms} \approx 40$ nV. Since the magnitude of the magnon-polaron resonance is typically $V_{TA} < 1$ μV, the fact that we do not observe any magnon-polaron resonance features in the ciSSE data could be due to the fact that V_{TA} is smaller than the noise floor in the ciSSE configuration.

Appendix F: Modelled magnetic field dependence

Figure 14 shows the magnetic field dependence of the nlSSE signal as obtained from the FEM for short ($d = 1$ μm), intermediate ($d = 8$ μm) and long ($d = 20$ μm) distance and for $\delta = 2.0$ (top panels) and $\delta = 0.5$ (bottom panels). The experimentally observed behavior, i.e. signal enhancement for short distance and signal suppression at long distance, is reproduced for $\delta = 0.5$ but not for $\delta = 2.0$. Note that only the magnon-polaron contribution[10] to the magnetic field dependence is included, neglecting the signal reduction resulting from the freeze out of magnons at large magnetic fields.

* These authors contributed equally to this work
† l.j.cornelissen@rug.nl
1 C. Kittel, Physical Review **110**, 836 (1958).
2 J. R. Eshbach, Journal of Applied Physics **34**, 1298 (1963).
3 E. Schlömann and R. I. Joseph, Journal of Applied Physics **35**, 2382 (1964).
4 A. Rückriegel, P. Kopietz, D. A. Bozhko, A. A. Serga, and B. Hillebrands, Physical Review B **89**, 184413 (2014).
5 N. Ogawa, W. Koshibae, A. J. Beekman, N. Nagaosa, M. Kubota, M. Kawasaki, and Y. Tokura, Proceedings of the National Academy of Sciences **112**, 8977 (2015).
6 A. Kamra, H. Keshtgar, P. Yan, and G. E. W. Bauer, Physical Review B **91**, 104409 (2015).
7 K. Shen and G. E. W. Bauer, Physical Review Letters **115**, 197201 (2015).
8 S. C. Guerreiro and S. M. Rezende, Physical Review B **92**, 214437 (2015).
9 T. Kikkawa, K. Shen, B. Flebus, R. A. Duine, K.-i. Uchida, Z. Qiu, G. E. W. Bauer, and E. Saitoh, Physical Review Letters **117**, 207203 (2016).
10 B. Flebus, K. Shen, T. Kikkawa, K.-i. Uchida, Z. Qiu, E. Saitoh, R. A. Duine, and G. E. W. Bauer, Physical Review B **95**, 144420 (2017).
11 J. Flipse, F. K. Dejene, D. Wagenaar, G. E. W. Bauer, J. B. Youssef, and B. J. van Wees, Physical Review Letters **113**, 027601 (2014).
12 M. Agrawal, V. I. Vasyuchka, A. A. Serga, A. D. Karenowska, G. A. Melkov, and B. Hillebrands, Physical Review Letters **111**, 107204 (2013).
13 M. Schreier, A. Kamra, M. Weiler, J. Xiao, G. E. W. Bauer, R. Gross, and S. T. B. Goennenwein, Physical Review B **88**, 094410 (2013).
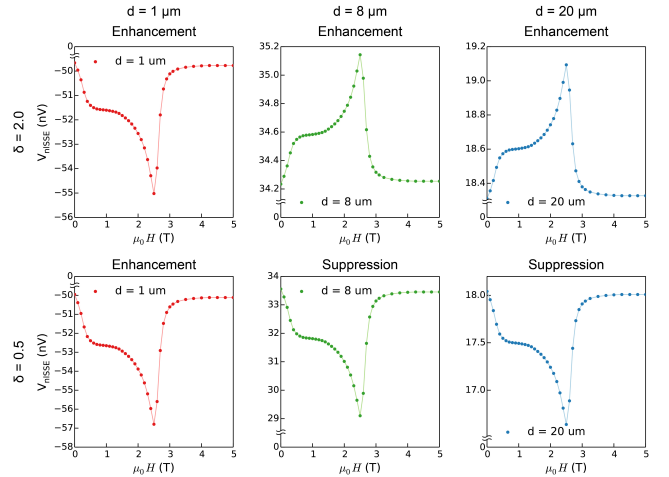
FIG. 14. Magnetic field dependence of the nlSSE signal obtained from the FEM. The results shown here are obtained for short ($d = 1$ μm), intermediate ($d = 8$ μm) and long ($d = 20$ μm) distance and for $\delta = 2.0$ (top panels) and $\delta = 0.5$ (bottom panels).

14 D. A. Bozhko, P. Clausen, G. A. Melkov, V. S. L'Vov, A. Pomyalov, V. I. Vasyuchka, A. V. Chumak, B. Hillebrands, and A. A. Serga, Physical Review Letters **118**, 237201 (2017).
15 F. Jedema, A. Filip, and B. van Wees, Nature **410**, 345 (2001).

[16] X. Lou, C. Adelmann, S. A. Crooker, E. S. Garlid, J. Zhang, S. M. Reddy, S. D. Flexner, C. J. Palmstrom, and P. A. Crowell, Nature Physics **3**, 197 (2007).

[17] N. Tombros, C. Jozsa, M. Popinciuc, H. T. Jonkman, and B. J. van Wees, Nature **448**, 571 (2007).

[18] I. Zutic, J. Fabian, and S. D. Sarma, Reviews of Modern Physics **76**, 323 (2004).

[19] L. J. Cornelissen, J. Liu, R. A. Duine, J. B. Youssef, and B. J. van Wees, Nature Physics **11**, 1022 (2015).

[20] S. T. B. Goennenwein, R. Schlitz, M. Pernpeintner, K. Ganzhorn, M. Althammer, R. Gross, and H. Huebl, Applied Physics Letters **107**, 172405 (2015).

[21] K. Ganzhorn, T. Wimmer, J. Cramer, S. Geprägs, R. Gross, M. Kläui, and S. T. B. Goennenwein, AIP Advances **7**, 085102 (2017).

[22] X. J. Zhou, G. Y. Shi, J. H. Han, Q. H. Yang, Y. H. Rao, H. W. Zhang, S. M. Zhou, F. Pan, and C. Song, Applied Physics Letters **110**, 062407 (2017).

[23] L. J. Cornelissen, J. Shan, and B. J. van Wees, Physical Review B **94**, 180402(R) (2016).

[24] L. J. Cornelissen and B. J. van Wees, Physical Review B **93**, 020403(R) (2016).

[25] A. V. Chumak, V. I. Vasyuchka, A. A. Serga, and B. Hillebrands, Nature Physics **11**, 453 (2015).

[26] K. Ganzhorn, S. Klingler, T. Wimmer, S. Geprägs, R. Gross, H. Huebl, and S. T. B. Goennenwein, Applied Physics Letters **109**, 022405 (2016).

[27] K. Uchida, J. Xiao, H. Adachi, J. Ohe, S. Takahashi, J. Ieda, T. Ota, Y. Kajiwara, H. Umezawa, H. Kawai, G. E. W. Bauer, S. Maekawa, and E. Saitoh, Nature Materials **9**, 894 (2010).

[28] N. Vlietstra, J. Shan, B. J. van Wees, M. Isasa, F. Casanova, and J. Ben Youssef, Physical Review B **90**, 174436 (2014).

[29] M. Weiler, M. Althammer, F. D. Czeschka, H. Huebl, M. S. Wagner, M. Opel, I. M. Imort, G. Reiss, A. Thomas, R. Gross, and S. T. B. Goennenwein, Physical Review Letters **108**, 106602 (2012).

[30] D. Meier, T. Kuschel, L. Shen, A. Gupta, T. Kikkawa, K. Uchida, E. Saitoh, J.-M. Schmalhorst, and G. Reiss, Physical Review B **87**, 054421 (2013).

[31] K. I. Uchida, H. Adachi, T. Ota, H. Nakayama, S. Maekawa, and E. Saitoh, Applied Physics Letters **97**, 172505 (2010).

[32] M. Schreier, N. Roschewsky, E. Dobler, S. Meyer, H. Huebl, R. Gross, and S. T. B. Goennenwein, Applied Physics Letters **103**, 242404 (2013).

[33] J. Shan, L. J. Cornelissen, N. Vlietstra, J. Ben Youssef, T. Kuschel, R. A. Duine, and B. J. van Wees, Physical Review B **94**, 174437 (2016).

[34] L. J. Cornelissen, K. J. H. Peters, G. E. W. Bauer, R. A. Duine, and B. J. van Wees, Physical Review B **94**, 014412 (2016).

[35] E. Saitoh, M. Ueda, H. Miyajima, and G. Tatara, Applied Physics Letters **88**, 182509 (2006).

[36] Z. Qiu, K. Ando, K. Uchida, Y. Kajiwara, R. Takahashi, H. Nakayama, T. An, Y. Fujikawa, and E. Saitoh, Applied Physics Letters **103**, 092404 (2013).

[37] F. L. Bakker, A. Slachter, J.-P. Adam, and B. J. van Wees, Physical Review Letters **105**, 136601 (2010).

[38] R. C. Lecraw and L. R. Walker, Journal of Applied Physics **32**, S167 (1961).

[39] I. H. Solt, Journal of Applied Physics **33**, 1189 (1962).

[40] B. Daudin, R. Lagnier, and B. Salce, Journal of Magnetism and Magnetic Materials **27**, 315 (1982).

[41] S. R. Boona and J. P. Heremans, Physical Review B **90**, 064421 (2014).

[42] J. Xiao, G. E. W. Bauer, K.-i. Uchida, E. Saitoh, and S. Maekawa, Physical Review B **81**, 214418 (2010).

[43] H. Adachi, K.-i. Uchida, E. Saitoh, and S. Maekawa, Reports on Progress in Physics **76**, 36501 (2013).

[44] S. M. Rezende, R. L. Rodríguez-Suárez, R. O. Cunha, A. R. Rodrigues, F. L. A. Machado, G. A. Fonseca Guerra, J. C. Lopez Ortiz, and A. Azevedo, Physical Review B **89**, 014416 (2014).

[45] S. M. Wu, J. E. Pearson, and A. Bhattacharya, Physical Review Letters **114**, 186602 (2015).

[46] G. A. Slack and D. W. Oliver, Physical Review B **4**, 592 (1971).

[47] T. Kikkawa, K.-i. Uchida, S. Daimon, Z. Qiu, Y. Shiomi, and E. Saitoh, Physical Review B **92**, 064413 (2015).

[48] H. Jin, S. R. Boona, Z. Yang, R. C. Myers, and J. P. Heremans, Physical Review B **92**, 054436 (2015).

[49] T. Kikkawa, K. I. Uchida, S. Daimon, and E. Saitoh, Journal of the Physical Society of Japan **85**, 065003 (2016).

[50] B. L. Giles, Z. Yang, J. S. Jamison, and R. C. Myers, Physical Review B **92**, 224415 (2015).